Journal of
Synchrotron Radiation

ISSN 0909-0495

Received 24 March 2006
Accepted 12 July 2006

Energy-dispersive absorption spectroscopy for hard-X-ray micro-XAS applications

S. Pascarelli,[a]* O. Mathon,[a] M. Muñoz,[b,a] T. Mairs[a] and J. Susini[a]

[a]European Synchrotron Radiation Facility, Grenoble, France, and [b]Laboratoire de Géodynamique des Chaînes Alpines, Université Joseph Fourier, Grenoble, France. E-mail: sakura@esrf.fr

Originally developed for time-resolved X-ray absorption spectroscopy (XAS), energy-dispersive absorption spectroscopy offers new opportunities for applications such as fluorescence detection and microbeams for scanning probe spectroscopy, thanks to recent developments in both instrumentation and optics. In this context, this paper presents a first example of chemical mapping recorded at ID24, the energy-dispersive XAS beamline at the ESRF. Attributes of this geometry for microanalysis are addressed. Finally, present and future plans are discussed and developed in the light of the evolution of the focal spot on this instrument in the past ten years.

Keywords: microspectroscopy; spectromicroscopy; X-ray absorption spectroscopy; XAS; energy-dispersive XAS.

1. Introduction

X-ray microanalysis techniques are evolving to address the development of nano-technologies by pushing spatial resolution (Adams *et al.*, 2005). As a result, there have been major developments in laboratory instruments and dedicated synchrotron beamlines worldwide (Cai *et al.*, 2000; Susini *et al.*, 2002; Marcus *et al.*, 2004; Somogyi *et al.*, 2005; Kagoshima *et al.*, 2004; Hirai *et al.*, 2004; Terada *et al.*, 2004; Flank *et al.*, 2006), and a very competitive context can be anticipated for the coming years. Towards this perspective, synchrotron-based analytical techniques (diffraction, imaging and spectromicroscopies) will play an important role by offering unique capabilities in the study of complex systems. Ultimately, this complexity can be envisioned in three directions: compositional, temporal and spatial. Typical experiments can be broadly divided into two categories: on the one hand, morphological studies, which require high spatial resolution and are, therefore, well adapted to two-dimensional or three-dimensional full-field imaging microscopy; on the other hand, studies dealing with co-localization and/or speciation of trace elements in heterogeneous systems. Scanning X-ray microprobes using various detection modes (transmission and fluorescence) are better suited for the latter cases, which often require both low detection limits and spectroscopic analysis capabilities for chemical composition and chemical state, respectively.

Compared with other techniques, synchrotron X-ray fluorescence (SXRF) microprobes display a unique combination of features (Ice, 1998). Today, SXRF microprobes using undulator sources provide micrometre spatial resolution and sub-p.p.m. detection limits for $Z > 20$. When associated with a high-efficiency detection system, the radiation damage is minimal, and accurate quantification is possible. Furthermore, the possibility of *in situ* experiments remains a unique attribute of synchrotron-based analytical methods. Physical penetration of hard X-rays enables specific sample environments to be developed to study realistic systems in their near-native environment rather than as 'model' systems. The ability to analyze *in situ* in environmental chambers such as high or low temperature, high pressure, or wet cells explains the increasing interest from communities such as planetary and earth sciences (*e.g.* Bassett *et al.*, 2000; Murakami *et al.*, 2004; Muñoz *et al.*, 2005), environmental science and microbiology (Lai *et al.*, 2004). More recently, fluorescence tomography has been developed, where two-dimensional slices are obtained through a three-dimensional object without physical sectioning (Golosio *et al.*, 2004; Vincze *et al.*, 2004).

The improvement of source stability of new synchrotrons together with the continuous advances in X-ray-focusing lenses is leading to further progress of submicrometre probes (Lengeler *et al.*, 2005; Schroer & Lengeler, 2005; Liu *et al.*, 2005; Hignette *et al.*, 2005; Maser *et al.*, 2004). However, if applied to X-ray absorption microspectroscopy (μ-XAS), optimal use of submicrometre probes are affected by two other factors: the angular stability of the energy-scanning crystal monochromator and possible photochemistry induced by the very high photon density in the nanoprobe.

Presently all operating μ-XAS beamlines worldwide are based on scanning XAS spectrometers, and feature full flux spot sizes of the order of a few micrometres FWHM. The major challenge for these instruments for two-dimensional μ-XAS mapping with a submicrometre resolution will be to stabilize the focal spot position as a function of energy. Early attempts of μ-XANES with a submicrometre beam (McHugo *et al.*, 2002) show how much of a challenge this is with a

scanning spectrometer. For chemical imaging purposes, where thousands of XAS spectra are to be collected for a single two-dimensional image, the position and energy calibration of the beam have to be kept stable for long periods of time, and while scanning the spectrometer rapidly. To give an order of magnitude, the beam time needed to map a 1 mm × 1 mm sample area with a spatial resolution of 1 μm (10^6 EXAFS spectra) exceeds 11 days at 1 s per spectrum. On the other hand, such an experiment becomes accessible with energy-dispersive XAS where acquisition times approach the ms per spectrum in transmission mode. The total beam time needed for the same map is less than 3 h at 10 ms per spectrum.

In this context, a submicrometre spot size on an energy-dispersive[1] XAS beamline optimized for both transmission and fluorescence detection stands out as a very powerful alternative, featuring a rigorously stable focal spot, in both position and shape, and rapid acquisition.[2]

Although the submicrometre scale is presently still not accessible, mainly due to limitations in the surface finish of X-ray optics, this paper aims at assessing various issues involved in the definition of a dispersive XAS beamline optimized for microanalysis on the micrometre scale. §2 gives a historical overview of the evolution of energy-dispersive XAS and applications. In this perspective, the energy-dispersive beamline at the ESRF is shown as an example, and described in detail in §3. The evolution of the spot size on this instrument, together with novel capabilities for X-ray fluorescence yield detection, suggested a specific development towards microanalysis applications, an example of which is illustrated in §4.

2. Evolution of energy-dispersive XAS spectrometers and their applications

The first design and evaluation of an energy-dispersive spectrometer to measure X-ray absorption fine structure (XAFS) spectra rapidly using synchrotron radiation was presented over 20 years ago (Matsushita & Phizackerley, 1981; Phizackerley *et al.*, 1983). The method employed a cylindrically bent triangular crystal to focus and disperse a quasi-parallel polychromatic X-ray beam onto the sample. The beam passing through the sample then diverged towards a linear photodiode array detector, where beam position could be correlated to energy. This method was applied successfully in the following years in the fields of biophysics, chemistry and materials science to track rapid changes in the local and electronic structure of absorber atoms in disordered systems (Matsushita *et al.*, 1986; Tourillon *et al.*, 1986; Ascone *et al.*, 1987; Yoshida *et al.*, 1990; Couves *et al.*, 1991).

In energy-dispersive XAS (ED-XAS) the time resolution for data acquisition is technically limited only by the readout time of the detection system, since all energy points are collected rigorously in parallel, and advances in time resolution closely followed developments in position-sensitive detectors (Iles *et al.*, 2000; Suzuki *et al.*, 2003; Newton *et al.*, 2005).

ED-XAS was found to be also well suited for studies at extreme conditions of pressure using a diamond-anvil cell (Itié *et al.*, 1989; Sapelkin *et al.*, 1996), where the strongly focusing crystal and the absence of movements provide the necessary small and stable focal spot, respectively. Moreover, from a practical point of view, Bragg reflections from the diamond anvils can be removed quickly from the energy range of interest, because the whole spectral range is observed simultaneously. The pressure range that can be covered has an upper limit defined by the size of the diamond culet, which is in turn limited by the size of the focal spot. Major breakthroughs occurred when the original triangular-shaped crystal bender was upgraded to the use of a profiled crystal (Tolentino *et al.*, 1990) and later to a profiled rectangular crystal on a four-point bender (Allen *et al.*, 1993). Further progress in X-ray focusing optics allowed the limit to be pushed up to the Mbar regime (San Miguel *et al.*, 2000; Pascarelli *et al.*, 2004; Aquilanti & Pascarelli, 2005).

Finally, the third application of ED-XAS takes full advantage of the intrinsic stability of this technique to collect data which inherently show only small differences, such as X-ray magnetic circular dichroism (XMCD) (Baudelet *et al.*, 1991). An important breakthrough in this field occurred with the extension of the use of quarter-wave plates to polychromatic and divergent beams (Giles *et al.*, 1994). Nowadays, ED-XAS is recognized as being a very valuable technique for XMCD studies at high pressures (Baudelet *et al.*, 1997; Mathon *et al.*, 2004).

Very recently, the ability of ED-XAS to detect very small differential signals has improved the sensitivity of extended X-ray absorption fine structure (EXAFS) measurements to include atomic displacements of the order of 0.00001 Å[3] (Pettifer *et al.*, 2005), which is about 100 times smaller than had previously been assumed. This was made possible by exploiting the stability (no moving parts) and acquisition speed of ED-XAS to overcome the major limitations of the conventional scanning EXAFS technique, *i.e.* the signal-to-noise ratio of the measurement and the energy stability between comparative measurements.

The conventional optical scheme for ED-XAS is shown in Fig. 1(*a*). The spectrometer is installed on a divergent synchrotron source (generally a bending magnet). The latter source naturally yields the large horizontal divergence (typically a few mrads) necessary to obtain, with reasonable radii of curvature of the polychromator crystal, an energy dispersion making it possible to cover a whole EXAFS spectrum.

[1] We will use the historically accepted term 'energy dispersive' throughout this paper, although the polychromator crystal performs more exactly a 'wavelength dispersion' of the incident beam.

[2] S. Pascarelli, O. Mathon, J. Susini, ESRF internal communication. A preliminary design for a hypothetical dispersive XAS beamline at the ESRF, that incorporates the future expected improvements in the quality of the optics, foresees a focal spot of the order of 300 nm × 300 nm.

[3] This value is obtained directly from the amplitude of the differential Fe *K*-edge EXAFS signal measured for an FeCo thin film undergoing periodic strain through magnetostriction. It represents, therefore, the sensitivity to atomic displacements, not to atomic positions.

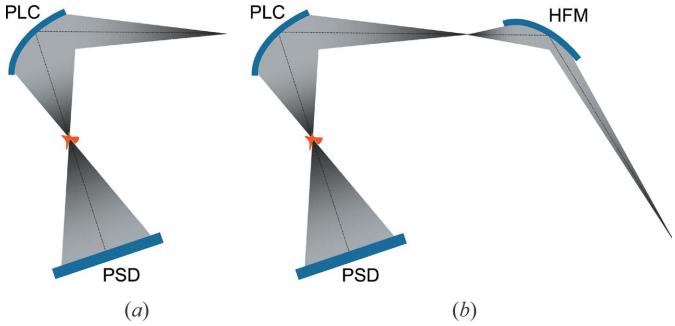

Figure 1
(*a*) The conventional optical scheme for ED-XAS. A source with a large divergence is used to maximize the footprint of the beam on the polychromator crystal (PLC). (*b*) The non-conventional optical scheme adopted on ID24, where a collimated undulator source is used. The necessary horizontal divergence is created using a strongly focusing mirror (HFM) upstream of the polychromator crystal.

Fig. 1(*b*) shows instead the non-conventional optical scheme adopted at the European Synchrotron Radiation Facility for beamline ID24, installed on an undulator source. The choice of an undulator is unusual, but has clear advantages (Goulon & Fontaine, 1991):

(i) The possibility of matching the bandwidth of emission of the undulator and the acceptance of the polychromator by optimizing the gap, the taper and the radius of curvature of the polychromator crystal. This results in a reduction of heat load on the optics.

(ii) A substantial reduction of unwanted harmonics.

(iii) Higher brightness and lower vertical divergence.

(iv) Low monochromatic horizontal and vertical divergences, which allow the optimal exploitation of the properties of quarter-wave plates to tune the helicity of incoming photons.

The required horizontal divergence is obtained by inserting a strongly focusing mirror upstream of the polychromator, as shown in Fig. 1(*b*). This mirror also performs a first important demagnification of the source making this optical scheme more suited for microfocus/high-brilliance applications. In conclusion, the unusual choice of an undulator source allows maximum advantage to be taken of a third-generation source.

3. Example of ID24

In this section we describe the optical scheme of ID24 and show the evolution of spot sizes in the past ten years. Such a consequential improvement has been possible thanks to an intensive research and development program carried out at the ESRF, often in collaboration with optics manufacturing companies. We indicate present limitations and possible evolution of the spot size in the future. Finally, we describe an option for sequential acquisition using an energy-dispersive spectrometer, which combines some of the advantages of the ED-XAS concept (*i.e.* small focal spot and stability of focus position and energy scale) with fast fluorescence detection.

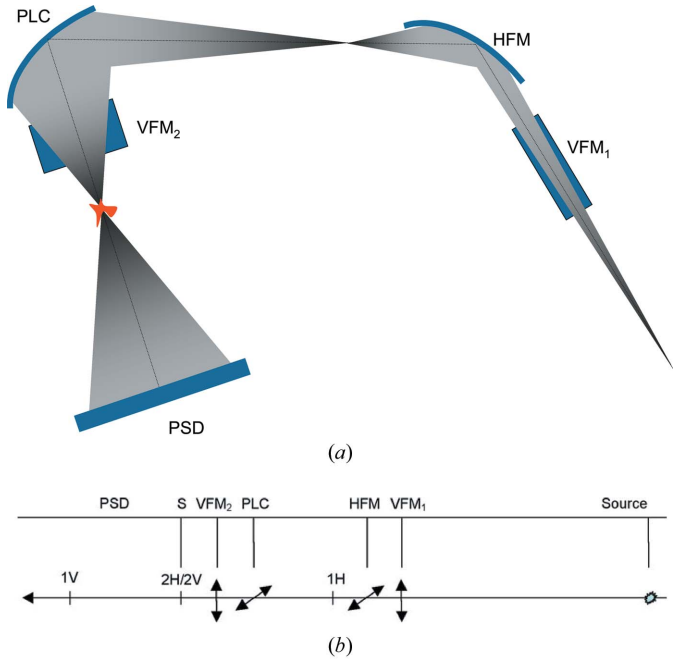

Figure 2
Top: the complete optical scheme adopted on ID24, consisting of a pair of mirrors in a Kirkpatrick–Baez geometry (VFM_1 and HFM) and the polychromator crystal (PLC). A second vertically focusing mirror (VFM_2) downstream of the polychromator is used to refocus the beam onto the sample. Bottom: schematic sequence of the focusing elements on ID24 (see text for details)

3.1. The optical scheme and evolution of spot size

Beamline ID24 at the European Synchrotron Radiation Facility represents the only example of the non-conventional scheme illustrated in Fig. 1(*b*). It uses undulator radiation emitted from two 42-pole undulators installed on a high-β straight section of the machine. The choice of a high-β section minimizes the mirror's length and therefore allows for better surface figure. The complete optical scheme of ID24 is shown in Fig. 2. The optics is based on the original configuration (Hagelstein *et al.*, 1997), *i.e.* a pair of mirrors in a Kirkpatrick–Baez geometry (VFM_1 and HFM) and the polychromator crystal (PLC). A second vertically focusing mirror (VFM_2) was added downstream of the polychromator (Pascarelli *et al.*, 2004) to refocus the beam on the sample. Mirror HFM demagnifies the source horizontally into 1H, the effective source for the polychromator crystal PLC.

Mirror VFM_1 slightly magnifies the source vertically into 1V, the effective source for VFM_2. The polychromator and VFM_2 then refocus the beam onto the sample position S horizontally and vertically, respectively (2H/2V). The shape and surface quality of VFM_1 and HFM have been optimized recently to reduce the spot size. Table 1 summarizes the present shape, slope error, positions and demagnification factors of the optical elements.

Fig. 3 illustrates the evolution of the size of the focal spot on ID24 in the past ten years. Discontinuities correspond to optimization of the optical scheme and elements (*i.e.* implementation of a profiled polychromator crystal (Pellicer-Porres *et al.*, 1998) and of the vertical refocusing mirror VFM_2,

Table 1
Shape, slope error FWHM values, positions and demagnification factors for the optical elements on ID24.

	Shape	Slope error (μrad) FWHM	p (m)	q (m)	q/p
VFM_1	Cylindrical	1.2	30	41	1.367
HFM	Elliptical	3.3	32.5	1.65	0.051
PLC	Elliptical	1.2	29.85	1.3	0.044
VFM_2	Elliptical	1.2	6	0.3	0.050

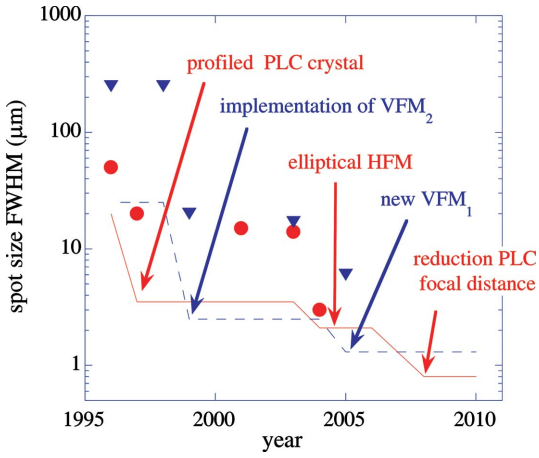

Figure 3
Measured FWHM values for the vertical and horizontal spot size are shown as triangles and circles, respectively. The dashed and continuous lines indicate estimated vertical and horizontal values in the limit of zero slope error on the optics, obtained directly from the demagnification factors listed in Table 1 and source sizes listed in Table 2.

followed more recently by the refurbishment of an elliptical HFM and a new VFM_1 both with state-of-the-art surface finish). In Fig. 3 we compare the measured spot sizes to estimated vertical and horizontal values in the limit of zero slope error on the optics, obtained directly from the demagnification factors listed in Table 1 and source sizes listed in Table 2. Estimates of final spot sizes, as well as the different contributions from source size and slope error, are listed in Table 3. The calculated values (in bold) are quite close (to within 30%) to the measured values shown in Fig. 3.

It is the quality of the polychromator crystal (surface polish and thickness homogeneity) which now limits the horizontal spot size: a thickness homogeneity better than ±2 μm along the 300 mm of the crystal can now be achieved leading to spot sizes as low as ∼3 μm FWHM measured at 15 keV (Fig. 4). In the vertical plane the spot size is presently still limited by slope errors on VFM_1. Measured values now are ∼6 μm FWHM (Fig. 5). In an upcoming refurbishment of the polychromator and experimental hutch, a reduction of the focal distance of the polychromator to ∼0.6 m is envisaged. This will have a double action: further decrease the horizontal spot and increase the energy window of the diffracted polychromatic beam, to yield a 1000 eV energy window sufficient to cover EXAFS at the Fe K-edge (7 keV).

In the limit of zero slope error on the optics, the estimated spot sizes are of the order of 2 μm × 1 μm FWHM. However, the surface finish of VFM_1 and of the polychromator are now

Table 2
Present values for the ID24 high-β section source size.

σ_i and σ_i' ($i = x, z$) refer to electron beam size and divergence, whereas Σ_i and Σ_i' ($i = x, z$) refer to source size and divergence including photon beam contributions.

	r.m.s.	FWHM
σ_x (μm)	402	945
σ_x' (μrad)	10.7	25.1
σ_z (μm)	7.9	18.6
σ_z' (μrad)	3.2	7.5
Σ_x (μm)	402	945
Σ_x' (μrad)	12.0	28.1
Σ_z (μm)	8.4	19.6
Σ_z' (μrad)	6.2	14.6

Table 3
FWHM dimensions of secondary sources and focal spots, including contributions due to source demagnification.

Values with and without slope-error contributions are shown.

	Source demag	Slope error	Secondary source FWHM (μm)	Secondary source demag	Slope error	Focal spot FWHM (μm)
Horizontal		HFM	Δx_{1H}		PLC	Δx_{2H}
	48.0	0.0	48.0	2.1	0.0	2.1
	48.0	10.9	49.2	2.1	3.1	**3.8**
Vertical		VFM_1	Δz_{1V}		VFM_2	Δz_{2V}
	26.8	0.0	26.8	1.3	0.0	1.3
	26.8	98.4	102.0	5.1	0.7	**5.1**

the limiting factors in spot size. In order to go below the micrometre, important modifications of the optical scheme as well as major advances in surface finish technology are required.

3.2. Fluorescence detection

In ED-XAS the beam impinging on the sample is polychromatic. The simultaneous absorption, by the sample, of polychromatic photons in a large energy range, as well as the conservation, upon interaction with the sample, of the photon energy–direction correlation, is at the basis of the parallel acquisition feature that characterizes ED-XAS and leads to unequalled time resolution (today, *circa* the ms for non-reversible processes). Therefore, core-hole decay spectroscopies, that imply the detection of emitted fluorescence photons or of total electron yield for each energy value of the absorbed photon, and where energy-direction correlation is not preserved, require a new strategy. Samples with low absorber concentration in highly absorbing matrixes, for example, are not suited for ED-XAS in the usual 'parallel acquisition' mode. This is also true for samples that produce important small-angle scattering, since the energy–direction correlation is strongly perturbed resulting in an important loss in energy resolution on the detector. The use of scattering filters to overcome this has been attempted (Hagelstein *et al.*, 1998).

The TurboXAS mode (Pascarelli *et al.*, 1999), whereby a thin slit positioned immediately downstream of the poly-

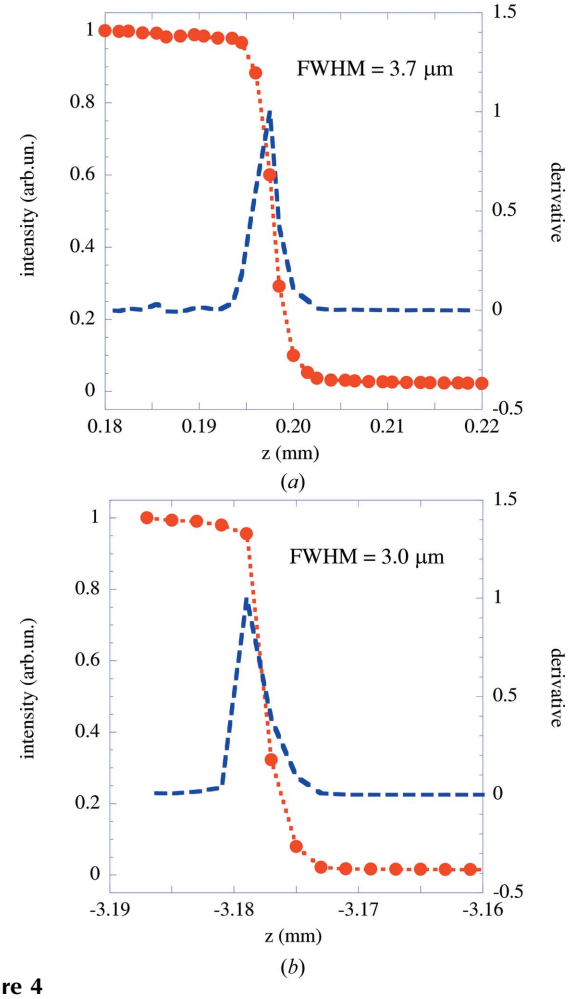

Figure 4
Horizontal knife-edge scans of the focal spot measured on ID24 at 7 keV (top) and 15 keV (bottom). The scan sampling is limited by the stepping-motor resolution (1 µm).

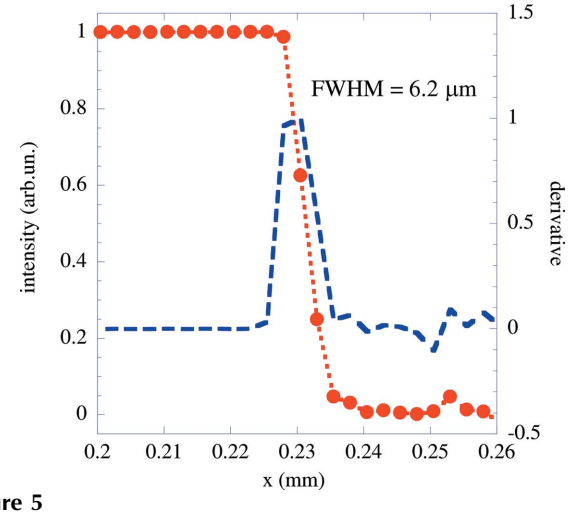

Figure 5
Vertical knife-edge scans of the focal spot measured on ID24 at 7 keV. The scan sampling is limited by the stepping-motor resolution (2 µm).

chromator selects a monochromatic beam from the polychromatic fan, makes it possible to take advantage of some of the features of ED-XAS, namely the energy and focal spot stability, to perform XAS on dilute samples using fluorescence detection, as well as subsecond XAS in transmission mode on samples not suited for parallel acquisition (Pascarelli *et al.*, 2000). This scheme was initially suggested by Oyanagi (1993). It is important to mention that this method only works on ID24 because the energy resolution contribution due to source size can be neglected with respect to other contributions, *i.e.* slit aperture and intrinsic energy resolution of the crystal. This is due to the presence of a small effective source for the polychromator (see Fig. 1*b*) which is not the general case of the conventional optical scheme depicted in Fig. 1(*a*).

TurboXAS is now routinely used for fast time-resolved XAS studies in operando conditions of dilute catalysts on highly absorbing matrixes, carried out by industrial groups[4].

A thin slit (∼100 µm) is scanned rapidly through the polychromatic fan, downstream of the polychromator crystal. The incident photon flux, I_0, is monitored using a first Si PIN diode on the scattered radiation by a Kapton foil. The total fluorescence yield is detected using a second Si PIN diode, I_F, oriented at $\pi/2$ with respect to the incident-beam direction. Acquisition time is limited by the signal-to-noise ratio. Typical dwell times are ∼1–2 s per XAFS spectrum. Spectra are acquired continuously as the slit is scanned along increasing and decreasing energies. The dead-time between spectra is dominated by positive and negative acceleration of the slit upon inversion of direction and is of the order of 300 ms. Dead-time between spectra can eventually be minimized by substituting the linear scanning slit with a continuously rotating spiral-shaped slit that spans the whole fan of radiation at every turn. With this implementation, acquisition rates can approach the 10 Hz regime, and will be limited in most cases by statistical noise on I_F.

4. Example of chemical mapping

As mentioned previously, the combination of a small spot size and fluorescence detection makes this instrument attractive for micro-analysis with a current spatial resolution below 10 µm. The aim of this preliminary experiment was to explore the practical feasibility of complete two-dimensional mapping of a natural sample, where each pixel contains full XANES information. It is worth noting that due to the absence of mechanical scanning of the monochromator (the slit motion does not affect the probe position, nor the energy calibration) the spatial resolution is not affected by the energy scan and remains fixed to the dimensions of the probe and the energy scale is preserved. Moreover, the dwell time per pixel is short enough to make it practically possible to acquire 100 pixel × 100 pixel images in a few hours. We performed a first test experiment at the Fe *K*-edge on a natural rock thin section (30 µm-thick sample glued onto a 1 mm-thick glass plate). This complex geological sample, where chlorite, phengite and quartz minerals were thought to coexist, was an excellent candidate because of (i) the high variations of iron content and (ii) the expected variations of iron redox and speciation.

[4] Unpublished proprietary research.

XANES spectra were collected in the fluorescence mode, and the covered energy range, from 7100 to 7200 eV, was acquired in about 1.5 s per spectrum. A region of interest of 390 µm by 180 µm covering the three different minerals was selected. The mapping was performed by horizontal and vertical steps of 5 µm so that 2808 XANES spectra were collected within about 100 min.

Although this approach generates a complete spectroscopic analysis, the data reduction had to be developed to produce images that give clear information on the chemical/structural properties of the sample. In particular, considering the amount of spectra to be treated, all the classical operations involved in XAFS data reduction (energy calibration, normalization, edge position tracking, extraction of fine structure *etc.*) had to be automatized and formatted as matrixes. A first approach of mapping reconstruction using this set of data is described by Muñoz *et al.* (2006).

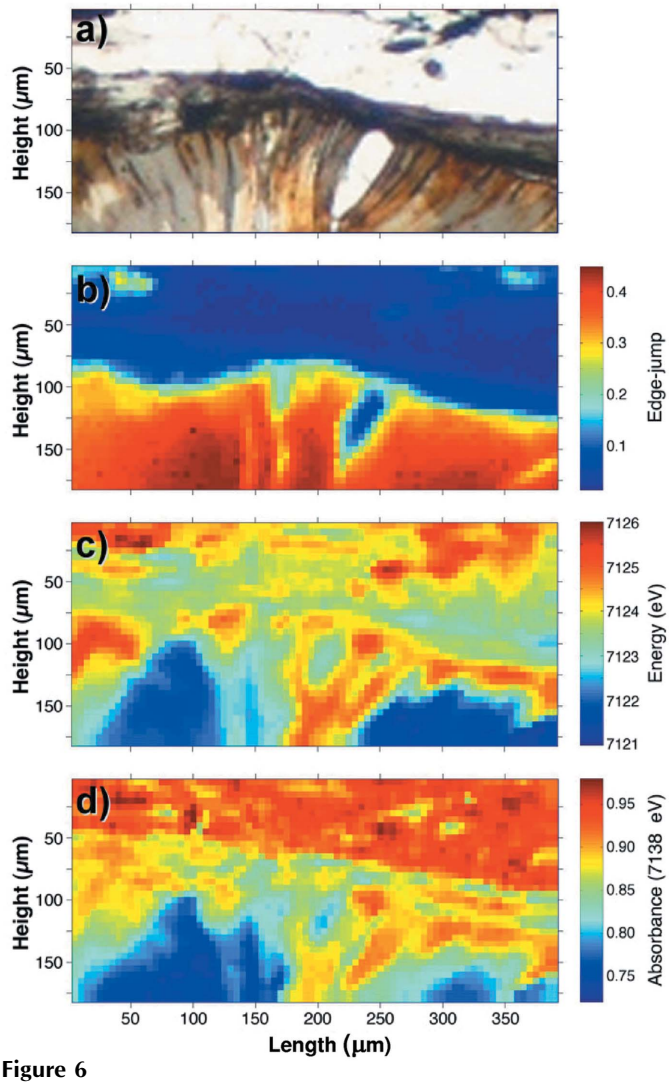

Figure 6
Images of the region of interest selected for a natural rock thin section. (*a*) Optical view showing the chlorite, phengite and quartz minerals, respectively, in the lower, middle and higher part of the image. (*b*) Qualitative iron content mapping, based on the edge-jumps of the XANES spectra. (*c*) Qualitative iron redox mapping, based on the position of the absorption edges of the XANES spectra. (*d*) Qualitative iron speciation mapping, based on the absorbance contrasts of the XANES spectra at 7138 eV.

Fig. 6(*a*) presents an optical image of the region of interest defined on the sample. Chlorite is the greenish-to-brownish mineral in the lower part of the picture, quartz is the white mineral located in the higher part, and phengite is the 'fibrous' mineral located in between chlorite and quartz. The edge-jump values provided by arctangent fits can be directly correlated to the total iron content of the sample, shown in Fig. 6(*b*). This image highlights qualitatively an important contrast between the different minerals. Iron content in chlorite appears particularly high and homogeneous, whereas phengite and quartz show, respectively, a low and very low iron content. Some complementary quantitative electronic microprobe analyses suggested, respectively, 24 wt%, 2 wt% and 2000 p.p.m. of iron in those different minerals. Such a high heterogeneity of iron content clearly highlights the three different crystalline phases.

Similarly, a mapping was reconstructed based on the position of the inflection points of the arctangents assimilated to the energy of the absorption edge (Fig. 6*c*), this criterion being directly correlated to the oxidation state of iron. The mapping reveals a relatively high iron redox contrast in the chlorite mineral, with a significant shift of the absorption edge (around 4 eV, from 7121 to 7125 eV). Thus, the blue regions mostly correspond to the presence of ferrous iron whereas red regions mostly correspond to ferric iron in chlorite.

A speciation mapping is finally presented in Fig. 6(*d*). This mapping is based on the variation of the absorbance at a selected energy for the normalized XANES spectra. Results show a good correlation with Fig. 6(*c*), suggesting that iron (II) and iron (III) are most likely localized in two different crystallographic sites into the chlorite mineral (see Muñoz *et al.*, 2006, for details).

Quantitative interpretation can be carried out based on an accurate analysis of the XANES and pre-edge regions of the spectra. This analysis requires generally a high signal-to-noise ratio to extract redox and speciation information. For this reason, XANES spectra belonging to the same entity (*e.g.* ferrous iron in chlorite) were averaged based on different 'masks' generated from the images (see Muñoz *et al.*, 2006). Fig. 7 presents a comparison, for the signals corresponding to ferrous and ferric iron in chlorite, between single- and averaged-pixel spectra. This figure illustrates that the quality of a 'single-pixel' XANES is comparable with the 'averaged-pixel' XANES (Fig. 7*a*) but that averaged spectra are required for extraction of quantitative information from pre-edges (Fig. 7*b*).

5. Conclusions

The case of ID24 has been used to illustrate the potential of an energy-dispersive spectrometer for micro-XAS applications. The advantages of an energy-dispersive spectrometer, that features no movement of optics during acquisition leading to an enhanced stability of energy scale, spot size and position, combined with a micrometre-sized spot and fluorescence

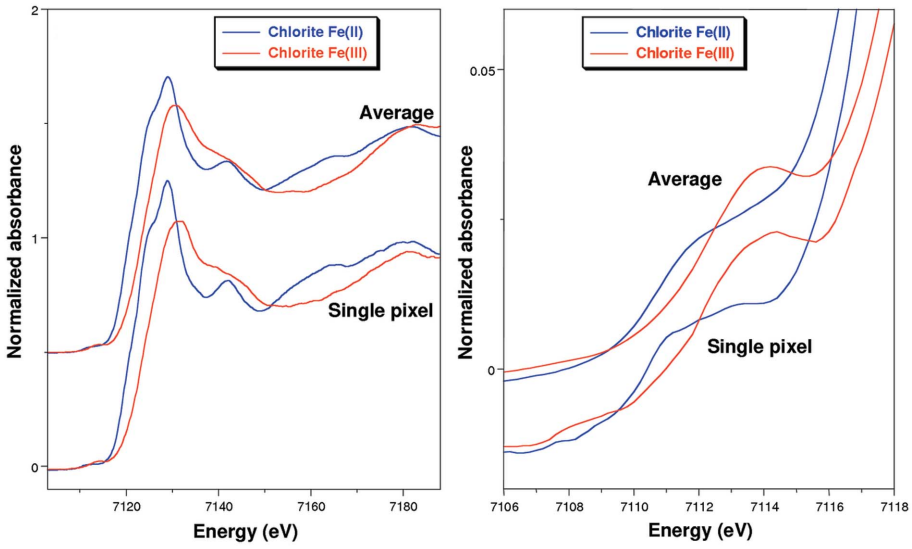

Figure 7
Qualitative signal-to-noise comparison between a single spectrum and the averages for the spectra from the Fe^{2+}- and Fe^{3+}-chlorite regions. (*a*) XANES spectra; (*b*) pre-edge regions.

detection, make it realistic to address two-dimensional mapping with micrometre resolution on heterogeneous samples, providing full XAFS information on each pixel. This information, intrinsically complete, is also too complex to be directly visualized. The extraction of the relevant information, spanning from simple oxidation state identification (from XANES) to local structural parameters (from EXAFS), will require specific software developments for data reduction, image reconstruction and visualization, providing targeted reduced XAFS information on each pixel.

In the years to come, improvements in crystal and mirror surface quality are expected and will allow 'ideal optics' values of the order of the micrometre for this beamline to be approached. In order to go beyond the micrometre, major modifications of the optical scheme are required, and a longer beamline, with higher demagnification, is to be envisaged.

We are very grateful to S. Pasternak for technical assistance in the design of the experimental set-up of all μ-XAS experiments on ID24. M. C. Dominguez and F. Perrin are greatly acknowledged for assistance in the acquisition software and electronics of the TurboXAS mode. We are also indebted to A. Vivo for endless assistance in the control, the diagnostics and the acceptance tests of the optical elements. We would like to thank P. Villermet and J. P. Vassalli for constant implication in the preparation of high-quality crystal polychromators. Finally, we thank the editor and the referees for constructive comments.

References

Adams, F., Van Vaeck, L. & Barrett, R. (2005). *Spectrochim. Acta*, B**60**, 13–26.
Allen, P. G., Conradson, S. D. & Penner-Hahn, J. E. (1993). *J. Appl. Cryst.* **26**, 172–179.
Aquilanti, G. & Pascarelli, S. (2005). *J. Phys. Condens. Matter*, **17**, 1811–1824.
Ascone, I. *et al.* (1987). *Springer Series in Biophysics*, Vol. 2, *Biophysics and Synchrotron Radiation*, edited by A. Bianconi and A. Congiu-Castellano. Berlin: Springer Verlag.
Bassett, W. A., Anderson, A. J., Mayanovic, R. A. & Chou, I.-M. (2000). *Chem. Geol.* **167**, 3–10.
Baudelet, F., Dartyge, E., Fontaine, A., Brouder, C., Krill, G. & Piecuch, M. (1991). *Phys. Rev. B*, **43**, 5857–5866.
Baudelet, F. Odin, S., Giorgetti, C., Dartyge, E., Itié, J.-P., Polian, A., Pizzini, S., Fontaine, A. & Kappler, J.-P. (1997). *J. Phys. IV*, **7**(C2), 441–442.
Cai, Z., Lai, B., McNulty, I., Khounsary, A., Maser, J., Ilinski, P., Legnini, D., Trakhtenberg, E., Xu, S., Tieman, B., Wiemerslage, G., Yun, W. & Gluskin, E. (2000). *AIP Conf. Proc.* **521**, 31–34.
Couves, J. W., Thomas, J. M., Waller, D., Jones, R. H., Dent, A. J., Derbyshire, G. E. & Greaves, N. (1991). *Nature (London)*, **354**, 465–468.
Flank, A.-M., Cauchon, G., Lagarde, P., Bac, S., Janousch, M., Wetter, R., Dubuisson, J. M., Idir, M., Langlois, F., Moreno, T. & Vantelon, D. (2006) *Nucl. Instrum. Methods Phys. Res. B*, **246**, 269–274.
Giles, C., Malgrange, C., Goulon, J., de Bergevin, F., Vettier, C., Dartyge, E., Fontaine, A., Giorgetti, C. & Pizzini, S. (1994). *J. Appl. Cryst.* **27**, 232–240.
Golosio, B., Somogyi, A., Simionovici, A., Bleuet, P., Susini, J. & Lemelle, L. (2004). *Appl. Phys. Lett.* **84**, 2199–2201.
Goulon, J. & Fontaine, A. (1991). ESRF Internal Report AF-JG/XAS/ESRF/02–91. ESRF, Grenoble, France.
Hagelstein, M., Lienert, U., Ressler, T., San Miguel, A., Freund, A., Cunis, S., Schulze, C., Fontaine, A. & Hodeau, J. L. (1998). *J. Synchrotron Rad.* **5**, 753–755.
Hagelstein, M., San Miguel, A., Fontaine, A. & Goulon, J. (1997). *J. Phys. IV*, **7**(C2), 303–308.
Hignette, O., Cloetens, P., Rostaing, G., Bernard, P. & Morawe, C. (2005). *Rev. Sci. Instrum.* **76**, 063709(1–5).
Hirai, Y., Yasuami, S., Kobayashi, A., Hirai, Y., Nishino, J., Shibata, M., Yamaguchi, K., Liu, K.-Y., Kawado, S., Yamamoto, T., Noguchi, S., Takahashi, M., Konomi, I., Kimura, S., Hasegawa, M., Awaji, N., Komiya, S., Hirose, T., Ozaki, S., Okajima, T., Ishikawa, T. & Kitamura, H. (2004). *Nucl. Instrum. Methods*, A**521**, 538–548.
Ice, G. E. (1998). *X-ray Microprobe for Fluorescence and Diffraction Analysis*, in *Methods in Materials Research: A Current Protocols Publication.* New York: John Wiley.
Iles, G., Dent, A., Derbyshire, G., Farrow, R., Hall, G., Noyes, G., Raymond, M., Salvini, G., Seller, P., Smith, M. & Thomas, S. (2000). *J. Synchrotron Rad.* **7**, 221–228.
Itié, J.-P., Polian, A., Calas, G., Petiau, J., Fontaine, A. & Tolentino, H. (1989). *Phys. Rev. Lett.* **63**, 398–401.
Kagoshima, Y., Koyama, T., Wada, I., Niimi, T., Tsisaka, Y., Matsui, J., Kimura, S., Kotera, M. & Takai, K. (2004). *AIP Conf. Proc.* **705**, 1263–1266.
Lai, B., Maser, J., Vogt, S., Paunesku, T. & Woloschak, G. E. (2004). *Int. J. Radiat. Biol.* **80**, 459–461.
Lengeler, B., Schroer, C. G., Kuhlmann, M., Benner, B., Guenzler, T. F., Kurapova, O., Zontone, F., Snigirev, A. & Snigireva, I. (2005). *J. Phys. D*, **38** A218–A222.
Liu, W., Ice, G. E., Tischler, J. Z., Khounsary, A., Liu, C., Assoufid, L. & Macrander, A. T. (2005). *Rev. Sci. Instrum.* **76**, 113701(1–6).
McHugo, S. A., Mohammed, A., Thompson, A. C., Lai, B. & Cai, Z. (2002). *J. Appl. Phys.* **91**, 6396–6405.

Marcus, M. A., MacDowell, A. A., Celestre, R., Manceau, A., Miller, T., Padmore, H. A. & Sublett, R. E. (2004). *J. Synchrotron Rad.* **11**, 239–247.
Maser, J., Stephenson, G. B., Shu, D., Lai, B., Vogt, S., Khounsary, A., Li, Y., Benson, C. & Schneider, G. (2004). *AIP Conf. Proc.* **705**, 470–473.
Mathon, O., Baudelet, F., Itié, J.-P., Polian, A., d'Astuto, M., Chervin, J.-C. & Pascarelli, S. (2004). *Phys. Rev. Lett.* **93**, 255503-1–255503-4.
Matsushita, T., Oyanagi, H., Saigo, S., Kaminaga, U., Hashimoto, H., Kihara, H., Yoshida, N. & Fujimoto, M. (1986). *Jpn. J. Appl. Phys.* **25**, L523–L525.
Matsushita, T. & Phizackerley, R. P. (1981). *Jpn. J. Appl. Phys.* **20**, 2223–2228.
Muñoz, M., Bureau, H., Malavergne, V., Ménez, B., Wilke, M., Schmidt, C., Simionovici, A., Somogyi, A. & Farges, F. (2005). *Phys. Scr.* T**115**, 921–922.
Muñoz, M., De Andrade, V., Vidal, O., Lewin, E., Pascarelli, S. & Susini, J. (2006). *Geochem. Geophys. Geosyst.* Submitted.
Murakami, M., Hirose, K., Kawamura, K., Sata, N. & Ohishi, Y. (2004). *Science*, **304**, 855–858.
Newton, M. A., Fiddy, S. G., Guilera, G., Jyoti, B. & Evans, J. (2005). *Chem. Commun.* pp. 118–120.
Oyanagi, H. (1993). *Jpn. J. Appl. Phys. I*, **32**, 861–864.
Pascarelli, S., De Panfilis, S. & Neisius, T. (2000). *Phys. Rev. B*, **62**, 3717–3721.
Pascarelli, S., Mathon, O. & Aquilanti, G. (2004). *J. Alloys Compds*, **362**, 33–40.
Pascarelli, S., Neisius, T. & De Panfilis, S. (1999). *J. Synchrotron Rad.* **6**, 1044–1050.
Pellicer-Porres, J., San Miguel, A. & Fontaine, A. (1998). *J. Synchrotron Rad.* **5**, 1250–1257.
Pettifer, R. F., Mathon, O., Pascarelli, S., Cooke, M. D. & Gibbs, M. R. J. (2005). *Nature (London)*, **435**, 78–80.
Phizackerley, R. P., Rek, Z. U., Stephenson, G. B., Conradson, S. D., Hodgson, K. O., Matsushita, T. & Oyanagi, H. (1983). *J. Appl. Cryst.* **16**, 220–232.
San Miguel, A., Libotte, H., Gaspard, J.-P., Gauthier, M., Itié, J.-P. & Polian, A. (2000). *Eur. Phys. J. B*, **17**, 227–233.
Sapelkin, A. V., Bayliss, S. C., Lyapin, A. G., Brazhkin, V. V., Itié, J.-P., Polian, A., Clark, S. M. & Dent, A. J. (1996). *Phys. Status Solidi B*, **198**, 503–508.
Schroer, C. G. & Lengeler, B. (2005). *Phys. Rev. Lett.* **94**, 054802(1–4).
Somogyi, A., Tucoulou, R., Martinez-Criado, G., Homs, A., Cauzid, J., Bleuet, P., Bohic, S. & Simionovici, A. (2005). *J. Synchrotron Rad.* **12**, 208–215.
Susini, J., Salomé, M., Fayard, B., Ortega, R. & Kaulich, B. (2002). *Surf. Rev. Lett.* **9**, 203–211.
Suzuki, A., Inada, Y., Yamagushi, A., Chihara, T., Yuasa, M., Nomura, M. & Iwasawa, Y. (2003). *Angew. Chem. Int. Ed.* **42**, 4795–4799.
Terada, Y., Goto, S., Takimoto, N., Takeshita, K, Yamazaki, H., Shimizu, Y., Takahashi, S., Ohashi, H., Furukawa, Y., Matsushita, T., Ohata, T., Ishizawa, Y., Uruga, T., Kitamura, H., Ishikawa, T. & Hayakawa, S. (2004). *AIP Conf. Proc.* **705**, 376–379.
Tolentino, H., Baudelet, F., Dartyge, E., Fontaine, A., Lena, A. & Tourillon, G. (1990). *Nucl. Instrum. Methods Phys. Res. A*, **289**, 307–316.
Tourillon, G., Dartyge, E., Fontaine, A. & Jucha, A. (1986). *Phys. Rev. Lett.* **57**, 603–606.
Vincze, L., Vekemans, B., Brenker, F., Falkenberg, G., Rickers, K., Somogyi, A., Kersten, M. & Adams, F. (2004). *Spectrochim. Acta*, B**76**, 6792–6796.
Yoshida, N., Matsushita, T., Saigo, S., Oyanagi, H., Hashimoto, H. & Fujimoto, M. (1990). *J. Chem. Soc. Chem. Commun.* **4**, 354–356.